Weld map tomography for determining local grain orientations from ultrasound

Michal Kalkowski, Michael Lowe, Vykintas Samaitis, Fabian Schreyer, Sébastien Robert

Weld map tomography for determining local grain orientations in welds from ultrasound

Michał K. Kalkowski[a,b,*], Michael J. S. Lowe[a], Vykintas Samaitis[c], Fabian Schreyer[d], Sebastien Robert[e]

[a] *Mechanical Engineering, Imperial College London, SW7 2AZ, UK*
[b] *Institute of Sound and Vibration Research, University of Southampton, SO17 1BJ, UK*
[c] *Prof. K.Baršauskas Ultrasound Research Institute, Kaunas University of Technology, K. Baršausko st. 59, Kaunas 51423, Lithuania*
[d] *Materials Testing Institute (MPA) University of Stuttgart. Pfaffenwaldring 32, 70569 Stuttgart, Germany*
[e] *CEA, LIST, Gif-sur-Yvette F-91191, France*

Abstract

The complex structure of inhomogeneous (e.g. austenitic stainless steel) welds poses a long-standing challenge in ultrasonic non-destructive testing. Elongated grains with spatially varying dominant orientations curve ultrasonic beams hindering the interpretation of inspection data. One way to tackle this problem is to include material information in imaging and signal analysis; however, such information is most often only gathered using destructive methods. This paper reports the development of a weld inversion strategy determining local grain orientations, based on a ray tomography principle. The considered approach does not rely on a macroscopic weld description but may incorporate it to facilitate inversion. Thanks to that, it is more general that other available approaches, but allows for reducing the complexity by accounting for known information at the same time. The methodology is demonstrated on both numerical and experimental examples. The experimental work focuses on mock-up samples from the nuclear industry and a mock-up specifically manufactured for the project sponsoring this research. The 'ground truth' for the latter comes from an EBSD evaluation, which is the most accurate (yet destructive) examination technique available. The paper concludes by presenting the benefit of the material information obtained from the reported inversion model for ultrasonic imaging.

1. Introduction

Ultrasonic inspection of inhomogeneous welds remains a significant challenge in the nuclear industry. Their distinctive microstructure – long columnar grains with preferential orientations varying across the weld – is responsible for a surge in complexity of ultrasound propagation. First, the ultrasonic beam no longer travels across straight paths, but follow the minimum propagation time principle resulting in curved,

*Corresponding author
Email address: m.kalkowski@soton.ac.uk (Michał K. Kalkowski)

complicated rays. Consequently, locating a defect based on the time of flight is no longer viable without detailed material information and a suitable propagation model. The second effect is grain scattering. When passing through the subsequent grain boundaries the ultrasonic energy is scattered leading to the loss of amplitude of the main beam (attenuation) and elevated structural noise. Other issues include, e.g. beam splitting, that is, emergence of a secondary beam at a grain boundary that gives rise to two strong scattered waves.

The above mentioned issues may be at least partially accounted for if material information is available. Such knowledge allows for correcting ultrasonic images, which could then consider true propagation times. It would also help interpret conventional inspection acquisitions by revealing true beam paths and potential scatterer locations [1]. Material information can be obtained from classical examination (e.g. metallography), microscope imaging (EBSD) or assuming a certain structure of the weld (e.g. the gold-standard MINA model [2] or the Ogilvy map [3]). Examination methods are destructive, costly and have no outlook to be applied to components on the plant. On the other hand, simplified weld description models cover limited ranges of cases and their parameters need to be tuned. An alternative is to use inversion based on ultrasound and extract the orientation information from the ultrasonic measurements directly. This concept was one of the premises underpinning the ADVISE project addressing the multi-faceted problem of ultrasonic inspection of complex structured materials, of which this research is a part.

It is widely accepted that to support ultrasonic testing, one does not need to consider detailed grain topology [4–6]. Instead, a macroscopic description is sufficient, where the grains are locally homogenised with a uniform orientation over a chosen grid (often between 1 and 2 mm). Columnar grains with similar preferential orientations can be approximated as a transversely isotropic material with the axis of material symmetry co-linear with the dominant orientation. Historically, macroscopic weld descriptions were developed first to improve the understanding of inspection results. While no inversion was performed, their parameters were assumed based on the examination data and practical experience. Such geometric models include the famous Ogilvy map [3], the layered arrangement [7] or the more basic approximation using only two angles by Langenberg et al. [8]. A refined orientation layout, linked to welding parameters came with the MINA model [2] which draws the information from the welder's notebook and captures the solidification processes in a phenomenological manner. All these approaches required assuming some if not all parameters, especially for a weld of which little was known.

The first attempts to use ultrasonic measurements for determining orientations aimed at updating weld description parameters mentioned above. For instance, Gueudre et al. [9] used evolutionary optimisation to guess the 'arbitrary' MINA parameters (remelting rates and tilt angles) based on the echodynamic curve. One problem with this approach is the uncertainty related to transducer coupling when measuring amplitudes, as well as the limited range of configurations it could cover. The same parameters were later determined from the time-of-flight maps by Fan et al. [10], also based on a genetic algorithm. Inversion

based on Bayesian updating and the Ogilvy map was conducted at the University of Bristol [11], where this approach estimated parameters of the Ogilvy model. Weld description constraints were removed in another Bayes-based work [12, 13], where the orientations were identified on a per-cell basis. While delivering promising results, the Bayesian approaches incurred significant computational costs which was deemed as one of their key shortcomings.

Recent advances in the availability of high computing power led to the development of approaches based on soft computing. Singh et al. proposed employing deep neural networks to determine the orientation maps based on a large simulated database of times of flight through different grain layouts [14, 15]. While this approach gives the promise of real-time application, it still requires a computationally expensive training stage, and does not exploit the physics of wave propagation through the heterogeneous material. An alternative method which takes the advantage of modern optimisation methods was developed by Menard et al. [16, 17]. Their focus is on optimising the amplitude of the TFM image around a postulated defect by adjusting the parameters of a macroscopic weld description. While the main outcome of the method is the enhanced TFM image (with improved defect signature location and the signal-to-noise ratio), a grain orientation map is delivered as a by-product.

Although the developments reported in the previous paragraph provided solutions to some challenges, they were often based on 'black-box' optimisers, requiring significant calculation cost, pre-identified defect area, or limited to a given macro weld description. To the authors' knowledge, physics-based inversion was not fully exploited for the applications of interest. Hence, we developed a ray inversion-based method for characterisation of inhomogeneous welds based on ultrasonic array data acquired at the surface. Compared to the prior work, this is a more general inversion approach with a stronger link to physics of wave propagation. Time-of-flight tomography is a known method applied in a variety of contexts, including the biomedical field, in e.g. breast tomography [18]. However, the materials considered in those problems are locally isotropic which is not the case in complex welds. To account for the material complexity and other practical differences, e.g. the sensor arrangement, we extended the classical ray inversion, and developed and validated a new approach, suited to inhomogeneous welds, referred to as weld map tomography.

The different aspects of the developed method are presented in more detailed in the remainder of this article. In the next section, we outline the Fermat principle-based forward model underpinning the inversion. Then, we recall the fundamentals of ray tomography for structures comprising isotropic materials and present the extension enabling local anisotropy to be accounted for. This is followed by discussing the details of the implementation of inversion for welds, including our two-stage approach and regularisation. The description is followed by examples - first a numerical example based on grain-scale finite element simulation of a real weld case from EDF; second, a set of experimental examples of industry relevant welds - two mock-ups from EDF and a weld specifically manufactured and characterised for the ADVISE project - based contact transducer array measurements.

2. Forward model

Weld map tomography matches the simulated ultrasound time-of-flight with the experimental target by adjusting model parameters. The forward model, predicting times-of-flight for a given layout of grain orientations is essential to the inversion. The most accurate, yet computationally expensive route is to use time-domain finite element simulations, extremely versatile with regard to the material structure and geometry. An alternative, offering potentially more efficient solution is to use a ray tracing model. Previous research on ultrasound in inhomogeneous welds [1, 10] used a ray stepping algorithm following scattering at fictitious grain boundaries according to a chosen step size. While accurate, it provided the dominant energy path for a given shoot angle (not a selected transmitter-receiver pair) and hence was difficult to be implemented in an efficient manner. One needed to compute a large range of shooting angles and interpolate to obtain the time-of-arrival at desired location.

A crucial functionality of a forward model in this context is to determine the time-of-flight between transducers directly, without the need for interpolation. This can be achieved by utilising the Fermat principle stating that the propagation path between two points is always such that the propagation time is minimal. This principle can be effectively used with efficient shortest path finding algorithms popular from the origins of computer science. Nowers et al. [19, 20] suggested using various incarnations of the Dijkstra method to model ultrasound in welds. The present model draws from that contribution but with some modifications to improve efficiency. Given its origins, the forward model used here is called the shortest ray path model (SRP).

Nowers et al. [19, 20] suggest using a randomly distributed set of nodes and a selected search radius to maximise the accuracy of the prediction. Our approach is based on the fact that the common macroscopic weld descriptions impose a regular grid structure, with local orientations varying from cell to cell. Propagation across each cell is determined by its assigned orientation and the incident angle. Moreover, the tomography algorithm itself is also typically programmed over a grid. Hence, we decided to use the regular grid arrangement of seeds in the forward model to maintain consistency across different stages of inversion. For the ray stepping model, edges of each grid cell are seeded according to a chosen resolution, and the paths connecting all points around the cell are candidate propagation path segments. It is worth noting that a single segment only crosses a single cell, that is segments belonging to different cells do not cross, except at their start or end points.

Fig. 1 shows an illustrative computational domain with a weld, isotropic parent materials to its left and right, and a set of sources and receivers. The cells generally represent different properties, but for the ray model they are discretised in the same way - using the same number of seeds along each edge. The number of seeds determines the angular accuracy of the model, i.e. the range of allowable angles for a ray passing through the cell. Fig. 2 schematically depicts this setup.

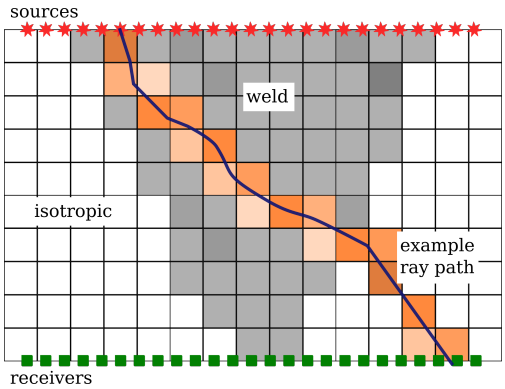

Figure 1: Computational representation of a weld in the SRP model. The orange-coloured cells represent those crossed by the depicted ray.

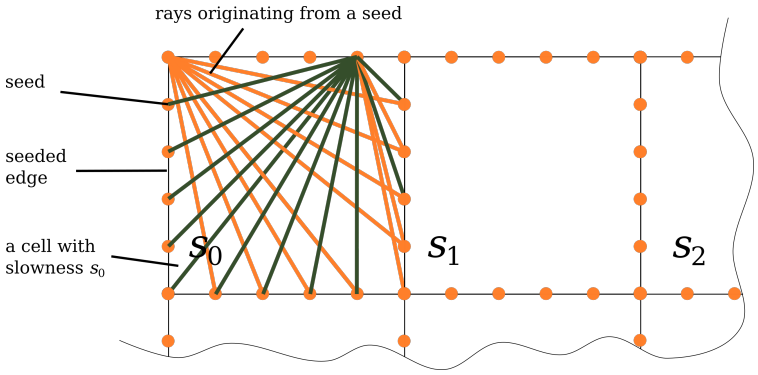

Figure 2: Seeding of cells in the SRP model. Two sets of cell rays are shown, for clarity, rays co-linear with the horizontal and vertical grid lines are not drawn.

The SRP model looks for the shortest propagation time between two chosen points. The propagation times across cells are calculated from the group slowness at given combination angles. The combination angles are a simple function of the local grain orientations and incident angles. Those propagation times are first computed for the whole model and fed into a shortest ray path algorithm (we used the `scipy.sparse.csgraph` [21] implementation).

One immediate advantage of the computational setup chosen is that rays within each cell have the same structure, e.g. they cover the same angles and have equal lengths. Therefore, they can be precomputed for a single cell and then used for the whole model. Further, this arrangement benefits from the common assumption allowing for using a single 'starting' elastic tensor for the weld. The homogenised elastic tensor in material coordinates is the same for the whole weld, but it is rotated on a cell-by-cell basis. The chosen construction of the SRP model only requires calculating a single group slowness as a function of the combination angle and delivers a quick calculation of the entire time-of-flight graph, offering significant computational advantages over the previously reported approaches.

The convergence study is not reported here for brevity, but for most considered cases, having 10 seeds for a 2 mm grid delivered good accuracy when compared with time-domain finite element simulations. This model, despite its high efficiency and versatility also has several limitations, related to its underpinning principle - the shortest propagation time between two points, not accounting for amplitude or energy. Consequently, it is unable to simulate beam splitting and secondary arrival times which sometimes may carry most of the energy. Further, it may output null paths, that is return ray paths associated with negligible energy transfer. However, these limitations do not affect the inversion algorithm as the inversion relies on measured arrival times. If arrival time for a certain transducer pair cannot be seen in measurements, it is not included in the inversion.

3. Ray inversion

This section covers the main elements of the ray inversion algorithm. It starts with a description of the better established methodology developed for materials with heterogeneous isotropy. The second subsection introduces the modifications needed to allow for anisotropy and variable grain orientations. The final part gives details about the implementation of this inversion model for an inhomogeneous weld.

3.1. Heterogeneous isotropic medium

The inversion model developed in the ADVISE project is motivated by the paper by Hormati et al. [18], who used a bent-ray simulation to construct an ultrasonic breast tomography method. The fundamental concept behind acoustic tomography is to recover local unknown properties from the characteristics of sound propagation through a medium. In a heterogeneous medium (even if locally isotropic) the sound takes generally curved paths between two points, depending on the local properties. It is convenient to use

slowness when describing propagation time, and in this case we focus on group slowness, as the method is based on tracking arrival times of finite wave packets generated by the transmitters. A generic time-of-flight is the integral of the group slowness along the propagation path

$$\tau = \int_{\Gamma} s \, \mathrm{d}l \tag{1}$$

where τ is the time, Γ is the propagation path, s is the slowness and $\mathrm{d}l$ is the infinitesimal length along the path.

The discretised domain used in the ADVISE SRP model allows for writing it as a discrete sum

$$\tau = \sum_{i=0}^{N} s_i l_i \tag{2}$$

where s_i and l_i are the local slowness and the local length of a ray passing a cell. As outlined earlier, the set of possible ray lengths is finite and the same for each cell. It is also worth noting, that a single ray typically passes only a small proportion of cells. Hence, if we cast this formulation into the matrix form

$$\tau = \mathbf{L}\mathbf{s} \tag{3}$$

with $\mathbf{L}$ being the ray-length matrix and $\mathbf{s}$ a vector describing slownesses across the whole model, one notices that $\mathbf{L}$ is a sparse matrix.

The inversion minimises a cost function with the aim of determining model parameters that match the simulated times-of-flight with those obtained from a measurement. The cost function used in this work takes the form

$$C = \sum_{i=0}^{M} \left(\tau_{i,\mathrm{model}} - \tau_{i,\mathrm{exp}}\right)^2 \tag{4}$$

where M is the total number of rays considered (i.e. the number of transmitter-receiver pairs).

The optimisation relies on the gradient of the cost function with respect to the model parameters (here: slowness distribution). To calculate this gradient, one needs to find the derivative of the time taken by a ray with respect to the slowness of a cell covered by this ray. From Eq. (2), we can write

$$\frac{\partial \tau}{\partial s_j} = \sum_{i=0}^{N} \left[\frac{\partial s_i}{\partial s_j} l_i + s_i \frac{\partial l_i}{\partial s_j} \right] \tag{5}$$

A key assumption here is that the ray path remains constant, irrespective of the local properties, i.e. $\partial l_j / \partial s_j = 0$. This is an approximation, but it simplifies the inversion considerably. The path variations will also be implicitly accounted for in subsequent iterations of the gradient stepping algorithm. The path invariance assumption removes the second component of the above sum, while the first simplifies when one notes that $\partial s_i / \partial s_j$ is only non-zero if $s_i = s_j$. Hence, the final expression for the derivative becomes

$$\frac{\partial \tau}{\partial s_j} = l_j \tag{6}$$

meaning that the derivative of the propagation time over the local slowness is simply the local ray length (the length of a section passing the considered cell).

One can now formulate the gradient of the cost function with respect to the local properties, using the chain rule,

$$\frac{\partial C}{\partial s_j} = \sum_{i=0}^{M} 2\left(\tau_{i,\mathrm{model}} - \tau_{i,\mathrm{exp}}\right)\left(\frac{\partial \tau_{i,\mathrm{model}}}{\partial s_j} - \frac{\partial \tau_{i,\mathrm{exp}}}{\partial s_j}\right) \tag{7}$$

We denote the difference between the arrival times from the model and from the measurement as the residual r_i and we note that the measured arrival times do not depend on the slowness distribution in the model, which leads to

$$\frac{\partial C}{\partial s_j} = \sum_{i=0}^{M} 2 r_i \frac{\partial \tau_{i,\mathrm{model}}}{\partial s_j} \tag{8}$$

where the last term can be replaced by l_i for a heterogeneous isotropic medium.

Hormati et al. [18] suggest using the nonlinear conjugate gradient algorithm to step along the gradient toward the desired model properties. This approach calculates the step size at each iteration and is capable of following narrow paths (ill-conditioned), taking the criss-cross pattern. The algorithm starts from an initial guess and calculates the gradient based on the computed ray lengths as outlined above. Each subsequent step follows the local descent direction

$$\Delta \mathbf{s}_n = -\nabla C(\mathbf{s}_n) + \gamma_n \Delta \mathbf{s}_{n-1} \tag{9}$$

where the δ_n parameters determines the effect of the preceding step and can be calculated using the Fletcher-Reeves or alternative formulae. It may happen that the stepping will not decrease the cost function. In such cases, a back-tracking line search algorithm ensures that the cost function is decreased enough. The algorithm iteratively decreases the step size by a chosen factor, until the cost function drop is less than a chosen threshold.

From the computational viewpoint, each step of the gradient stepping approach requires solving the forward model once to obtain the gradient. If back-tracking line search is necessary, each iteration takes another forward solution. These offer a very efficient setup, with the number of forward solutions usually not much greater than the number of steps. This is thanks to the convenient expression for the gradient developed above.

3.2. Heterogeneous anisotropic medium

The ray inversion method described in the previous section assumes that each cell represents an isotropic medium. On the other hand, anisotropy is one of the key characteristics of inhomogeneous welds, and therefore, the algorithm needs to be extended to be suitable. For heterogeneous anisotropy the local group slowness is a function of the incident angle and the local grain orientation. Hence, the model parameters to

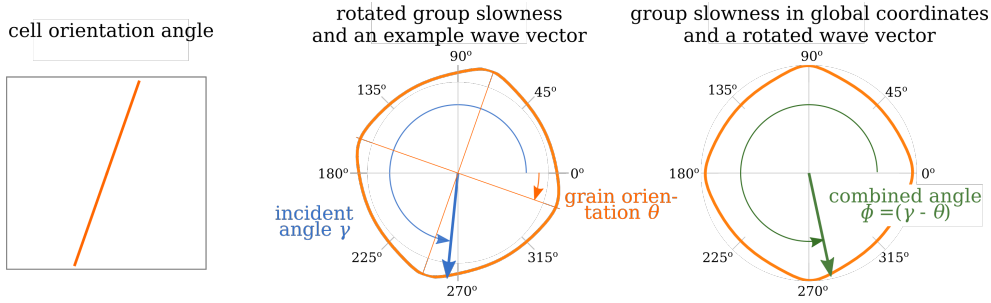

Figure 3: Group slowness for a transversely isotropic material - how the incident angle and grain orientation form a combined ray angle in material coordinates.

be determined using inversion are now local grain orientation, assuming that all cells can be described with one elastic tensor, appropriately rotated cell-by-cell.

To benefit from the characteristics of the grid - identical regular cells - one needs to express the local slowness for a given ray in material coordinates. Since all cells share the same 'basic' tensor, the group slowness curve is simply only rotated from cell to cell. Hence, the combined angle is a difference between the incident angle and the local orientation. Fig. 3 schematically depicts the angles involved and illustrates how the combined angle is formed.

The algorithm requires an expression for the gradient of the cost function with respect to local orientations. Let us first consider the derivative of the time-of-flight along a given ray. The slowness is now a function of both the incident angle and local grain orientation; however, under the path invariance assumption stated in the preceding section, only the dependence on grain orientation is retained. Hence, we write

$$\frac{\partial \tau}{\partial \theta_j} = \frac{\partial \tau}{\partial s_j}\frac{\partial s_j}{\partial \phi_j}\frac{\partial \phi_j}{\partial \theta_j} \tag{10}$$

where $\partial\tau/\partial s_j = l_j$, as previously shown, $\partial\phi_j/\partial\theta_j = -1$, since $\phi_j = \gamma_j - \theta_j$, and $\partial s_j/\partial\phi_j$ can be precomputed at the beginning, and interpolated as a callable function, as it stays the same for all cells. The derivative of the ray time-of-flight over local orientation finally is

$$\frac{\partial \tau}{\partial \theta_j} = -l_j \frac{\partial s_j}{\partial \phi_j}\Big|_{\text{at } \phi_j = \gamma_j - \theta_j} \tag{11}$$

This expression determines the form of the cost function gradient expression which is the core of the inversion model:

$$\frac{\partial C}{\partial \theta_j} = \sum_{i=0}^{M} -2 r_i l_j \frac{\partial s_j}{\partial \phi_j}\Big|_{\text{at } \phi_j = \gamma_j - \theta_j} \tag{12}$$

It is worth noting that the new term needs to be evaluated for each ray separately at every pixel, which adds complexity and computational cost to the isotropic solution, but these are in part minimised by the computational arrangement that takes the advantage of the regular grid structure.

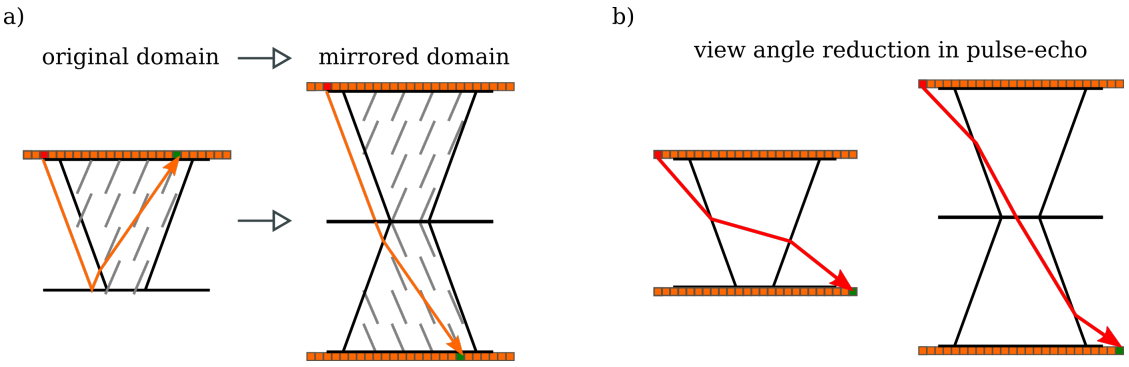

Figure 4: Auxiliary mirrored domain for inversion through the backwall: a) the setup; b) illustration of the reduction of the view angle between through-transmission and pulse-echo.

3.3. Implementation for an inhomogeneous weld

The weld inversion algorithm described above and the the forward SRP model were developed and coded in Python. The algorithm is generally applicable to generally anisotropic media, however its application to inhomogeneous welds gives a specific flavour to several aspects. They are briefly outlined below.

3.3.1. Material structure and elastic tensor for the weld

Most parent materials joined using the welds of interest to this paper can be modelled as isotropic. Hence, a typical inversion setup considered in the ADVISE project is solving only for grain orientations within the weld, with the parent material isotropic properties assumed a priori. The 'basic' transversely isotropic elastic tensor governing the columnar grain structure of the weld is considered constant, i.e. only the orientations are allowed to vary. This assumption allows for simplifying the computational domain and discretising only the weld region, considerably reducing the size of the graph along which the shortest path is of interest.

3.3.2. Transducer configuration

Transducer configuration is a challenge for weld map tomography. The classical tomography setup (both optical and acoustic) assumes a circular array of transmitter-receivers, ensuring a full coverage of view angles. Any setup different from the full view incurs considerable loss in the ability to recover the properties of the medium. Since weld map tomography relies on measured arrival times, one can realistically consider three configurations – (i) a through-transmission setup, with transducers on both the top and bottom surfaces; (ii) a pulse echo setup, with only one array on top of the weld; or (iii) a tandem configuration with two arrays located on the top surface on both sides of the weld. The illustration of the implication of the reduced view for the through-transmission and the pulse-echo setup can be found e.g. in [22].

The through-transmission setup is straightforward for the considered model, as the sources and receivers are places along the two edges of the computational domain. However, the pulse-echo and the tandem setup cannot be modelled directly. To account for the reflection from the backwall with the SRP model, one needs

to considered an extended domain, mirrored around the backwall. Note that not only the nodes but also material properties, including orientation angles need to be flipped. This technique is a direct consequence of the Fermat principle invoked in the preceding section. Fig. 4 schematically depicts the arrangement when through-backwall propagation is considered.

3.3.3. Incorporating the known information and regularisation

Weld map tomography is an ill-posed problem with multiple minima. Compared to the isotropic setup, the added complexity of the anisotropic weld context comes from the fact that the group slowness is not unique with respect to the ray angle. Hence, without incorporating additional information the inversion is likely to fail. Such input is possible both in the form of an educated initial guess/starting point for inversion and regularisation.

The grain layout of inhomogeneous welds is linked to the manufacturing procedure and the physics of solidification. These factors are at the origin of the previously mentioned weld models, such as MINA or the Ogilvy map. Whilst fast and effective, these models are constrained by the assumptions and simplifications. We suggest to take advantage of these models by using them as initial guesses for inversion. With the expectation that the inversion will target variations of the angles from this starting point, there is a higher chance of convergence compared to the case where the starting angles are random.

Likewise, metallography/EBSD examinations of welds show that the variation of angles is typically smooth with just a few abrupt changes. The orientations, following welding passes, tend to form regions with similar dominant orientations which vary smoothly across the cross section. Hence in many cases adding total variation and smoothness regularisation terms helps achieve convergence and reduce the risk of being trapped in non-physical local minima.

The analysis of destructive examinations suggest that often there exists a dominant orientation of grains. For the simplest symmetric cases, this will be the vertical direction, i.e. perpendicular to the surface. For other welds it may be a line almost parallel to the chamfer. This dominant orientation affects the propagation path considerably, and one approach to take advantage of this knowledge is to divide the inversion into two stages. Starting from the conventional Ogilvy map, in the first stage the algorithm is only adjusting the dominant orientation, that is, a single angle. When converged, it proceeds to updating local orientations across the weld. This approach was found particularly effective in our work and represents a pragmatic balance between the flexibility of ultrasonic tomography and the knowledge about the structure and the behaviour of welds of interest. This approach required a modification of the Ogilvy model, referred to as the 'generalised Ogilvy map', similar to that used in [17], which is described in more detail in Section Appendix A.

4. Numerical example

4.1. Microstructure and forward models

Having outlined the conceptual principles of weld map tomography, the attention now turns to examples. First, we present a numerical example in which the target times-of-flight came from grain-scale time-domain finite element simulations. The calculations were executed on a graphical processing unit (GPU) using Pogo, a fast GPU finite element solver developed at Imperial College London [23]. The example is motivated by a real industrial inspection case at EDF, France. The grain structure of the weld bent and split the incident ultrasonic beam, so that the reflection from the backwall at some locations could be misinterpreted as a defect. At the time, to support the interpretation of the inspection, a macroscopic weld description was created, based on metallography. We used that macroscopic descriptions to create a numeric microstructure, allowing us to capture the rich physics of ultrasound propagation through complex welds in simulation.

The model was generated using free polycrystal generation package – `neper` [24]. First, we created a vertically oriented columnar grain microstructure by stretching a standard Poisson-Voronoi tesselation along one dimension. Then for each orientation zone, the starting model was rotated and cropped according to the weld description from EDF. Each zone was accompanied with an individually generated set of crystallographic orientations which were randomly distributed along the dominant orientation (referred to as 'fiber' orientations in `neper`). The final step was comprised of stitching the microstructures for each zone into a complete weld representation. The starting macroscopic weld descriptions and the grain-scale model are shown in Fig. 5.

The generated microstructure was the basis for setting up the grain-scale finite element model, which is the virtual experiment in this section, depicted schematically in Fig. 6. The weld region was surrounded by isotropic regions, representing the parent plates ($c_{11} = 260\,\mathrm{GPa}$, $c_{12} = 100\,\mathrm{GPa}$, $c_{44} = 80\,\mathrm{GPa}$, $\rho = 8000\,\mathrm{kg\,m^{-3}}$). For each grain belonging to the weld, we rotated the crystal elasticity matrix (cubic crystal, $c_{11} = 206\,\mathrm{GPa}$, $c_{12} = 133\,\mathrm{GPa}$, $c_{44} = 119\,\mathrm{GPa}$, $\rho = 8000\,\mathrm{kg\,m^{-3}}$) according to Euler angles generated in `neper`. We simulated the action of a 64-element 2 MHz array on top of the weld by a series of vertical nodal forces (one force per element) separated by the pitch distance and acting on the top boundary of the weld with a 3-cycle toneburst time history. To minimise the impact of the finite computational domain and eliminate reflections, we used absorbing regions around the whole domain (except the backwall). The discretisation used a regular quad mesh (CPE4-type linear elements) with element size of 0.025 mm, which was a very conservative choice providing more than 100 elements per longitudinal wavelength. The time step was chosen based on the Courant number of 0.9, giving 3.7 ns. The model had nearly 12 million degrees of freedom, but was solved efficiently using Pogo [23] on a GPU card (illustrative solution times for one array shot with over 6800 time steps: standard gaming card Nvidia GTX 1080Ti – 15 s, Nvidia RTX 2080Ti – 10 s).

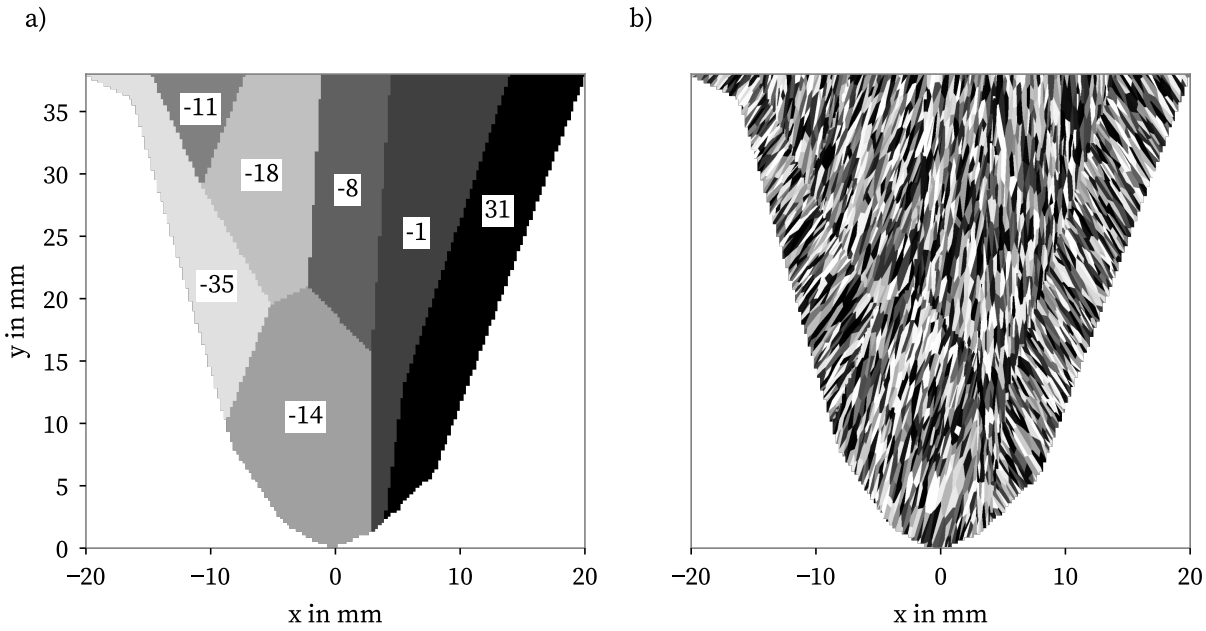

Figure 5: The macroscopic weld description with dominant orientations for each zone marked (a), and the generated synthetic microstructure (b) for the numerical example of weld map tomography. The orientations are quoted in degrees, measured from the vertical direction, with positive angles going anti-clockwise

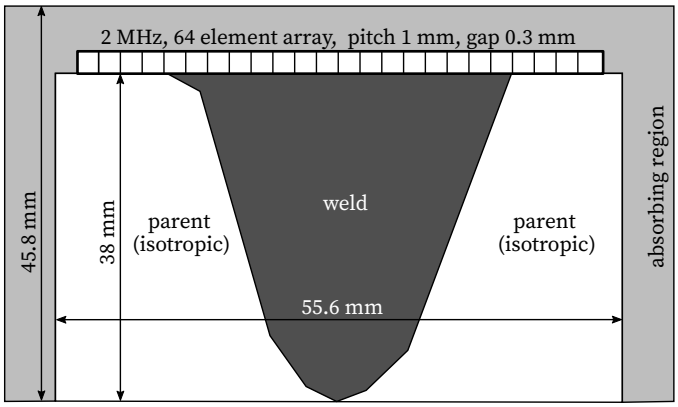

Figure 6: Schematic diagram for the FE model for the numerical example of weld map tomography.

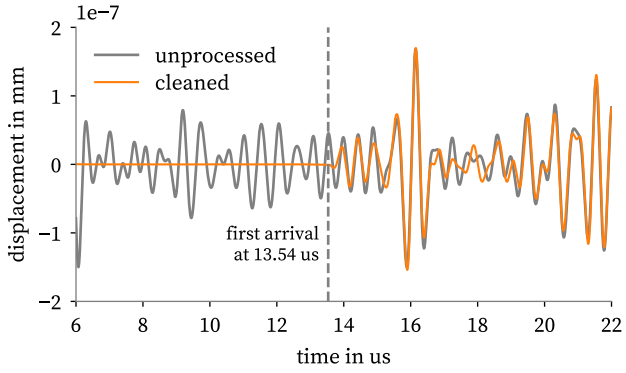

Figure 7: Illustrative simulated time trace for the numerical example - array element #41 transmitting and element #36 receiving.

Weld map tomography, as used in this paper, is based on backwall-reflected first arrivals, that is, longitudinal waves. To simplify extracting them from simulation, we executed an auxiliary calculation in which the backwall was replaced by an absorbing boundary. Substituting the two datasets led to clean first arrivals at the top surface. Such an approach is of course impossible in practice, but helps focus solely on the inversion algorithm, rather than peripheral issues, in a numerical example. Fig. 7 shows an example time trace and both unprocessed and cleaned signals, and the estimated arrival time. The estimation used an implementation of the Akaike Information Criterion [25] which helps if the first arrival is not the strongest in amplitude. For experimental datasets, obtaining an automated universal procedure is a research challenge on its own, and to keep the focus on inversion, we took the advantage of manual input.

To run the inversion on the simulated ultrasonic data, we first set up the SRP ray tracing model. The domain was cast on a regular 1 mm grid to accommodate weld geometry. The edges of each cell were seeded with ten nodes, and, to take the computational advantage described in Section 2, the algorithm pre-calculated the potential paths across a cell which were then used in all subsequent tracing. The domain was mirrored around the backwall, so that the pulse-echo configuration can be simulated. The SRP model is based on homogenisation, that is, it does not consider individual grains, but assigns local material properties based on the average grain orientation. Regions with columnar grains aligned to the same dominant angle are known to behave like a transversely isotropic material [6]. We exercised a homogenisation calculation based on the numerically generated microstructure, knowing that the dominant orientation should align with the direction of the smallest stiffness. The homogenisation yielded the following transversely isotropic material constants: $c_{11} = 248\,\mathrm{GPa}$, $c_{12} = 91\,\mathrm{GPa}$, $c_{13} = 133\,\mathrm{GPa}$, $c_{33} = 206\,\mathrm{GPa}$, $c_{44} = 119\,\mathrm{GPa}$, $c_{66} = 77\,\mathrm{GPa}$, and the same density as for the parent material $\rho = 8000\,\mathrm{kg\,m^{-3}}$. The vertically oriented grains have the 33 material axis aligned with the global z axis. Orientation angles are measured from the vertical, positive anticlockwise. A short note on the orientation convention is included in Section Appendix B. Note also

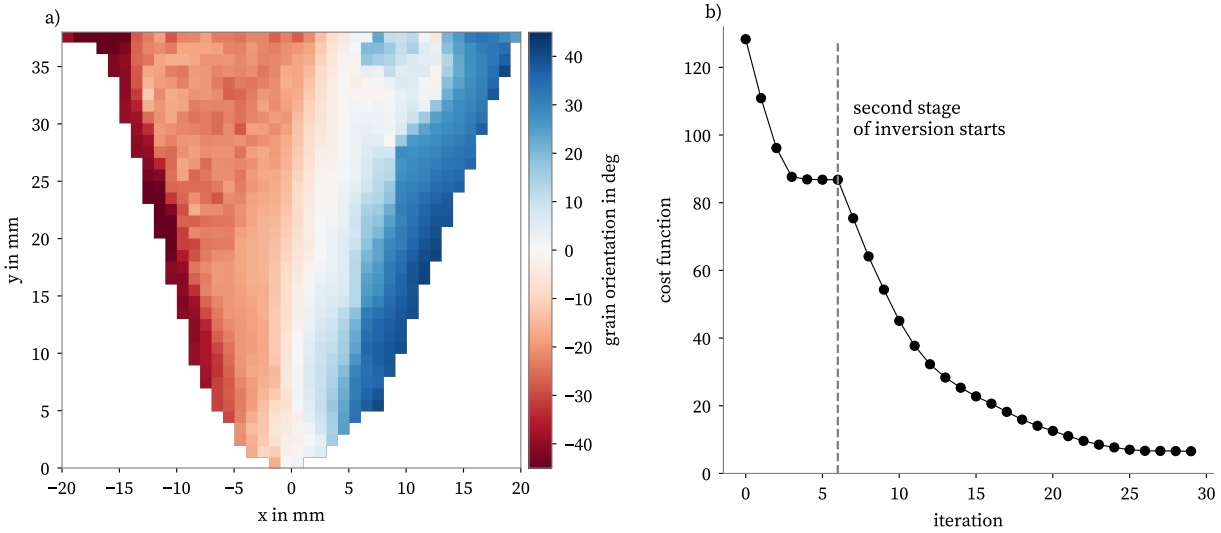

Figure 8: The result of weld map tomography based on time traces from grain-scale finite element simulations: a) obtained grain orientations; b) the cost function.

that the SRP model is set up in the y-z domain with z being the vertical, while the FE model is in the x-y domain.

4.2. Inversion

We used the two-stage inversion described above. The algorithm started with a 'standard' Ogilvy map ($T_L = T_R = n_L = n_R = 1$, $\alpha_L = \alpha_R = 20$) with a vertical dominant orientation ($\zeta = 0°$), converging to $-4.7°$ after six iterations. In the per-cell inversion stage we used smoothing and total variation regularisation, achieving convergence after a further 23 iterations.

Fig. 8 shows the obtained weld map and the evolution of the cost function. The vertical line marks the point where the first stage, in which only the dominant angle was varied for a general Ogilvy map, was completed. Individual orientations were then updated to the point where for the three consecutive iterations the cost function dropped by less than 2% (this criterion was adopted for both stages). The weld map can be compared to the original microstructure in Fig. 5.

Detailed error maps for the absolute angular error and the time-of-flight error are presented in Fig. 9. The mean, median, and maximum absolute angular errors ($|\theta_{\text{original}} - \theta_{\text{inversion}}|$) are 7.28, 5.71, and 33.06°, respectively. From a practical viewpoint, these are good results, compared to commonly reported average errors exceeding 20° [10]. We also compared the converged time-of-flight map to that chosen as a target for inversion in Fig. 9(b). The mean, median, and maximum absolute time errors ($|\tau_{\text{original}} - \tau_{\text{inversion}}|$) are 0.03, 0.02, and 0.27 µs, respectively.

The numerical example demonstrates the potential of weld map tomography and quantifies its performance. While errors exist, they are below the commonly reported level (as expected from a simulation-based

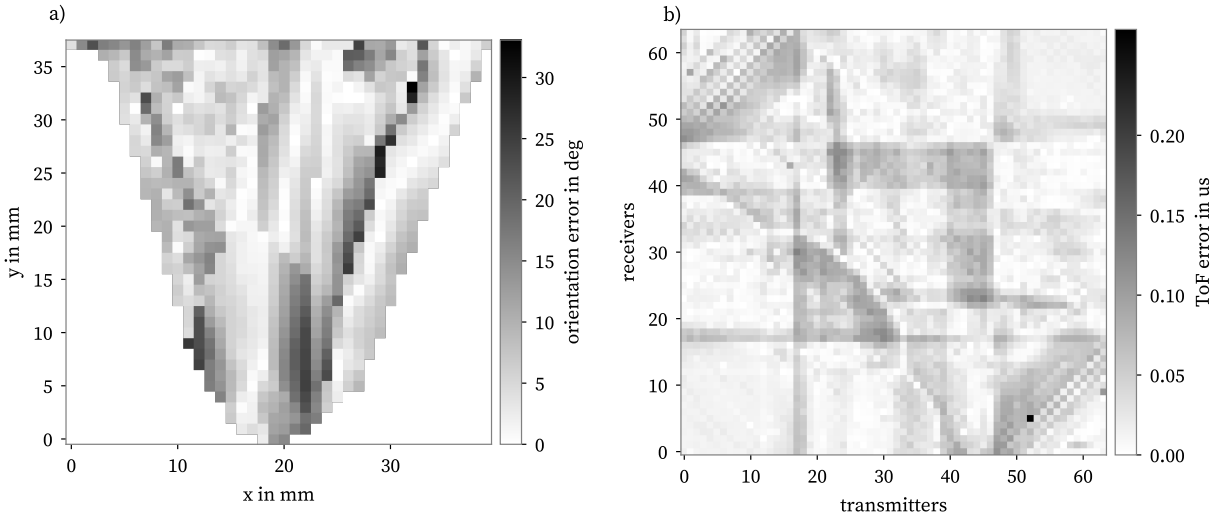

Figure 9: Error maps of weld map tomography based on time traces from grain-scale finite element simulations: a) orientation errors; b) time of flight errors.

study) and related to the limitations of time-of-flight tomography itself.

5. Experimental examples

In this section we report exercising weld map tomography on three experimental samples - two industrial mock-ups from EDF and one mock-up specifically manufactured for the ADVISE project. All samples had artificial defects created for testing imaging algorithms. Verifying the effectiveness of the inversion directly is not straightforward, as usually destructive material examinations are taken over a different part of the weld than that used in the measurement. But it is widely accepted in the community that grain orientations do not vary significantly along the weld, except for arc ends. Nevertheless, in a practical scenario, the best evaluation of the obtained weld structure information is its application to imaging. Hence, for all numerical examples, we demonstrate how the result of weld map tomography improves ultrasonic array images and the signatures of target defects.

5.1. Weld with uniform orientations

First, we consider a homogeneous Inconel 182 wide chamfer weld from EDF, with approximately uniform orientations, as used in [16]. Fig. 10 shows a photograph and a schematic diagram of the experimental pulse-echo setup used for inversion. As opposed to [16], we used contact measurements, with the array (5 MHz 64-element; pitch 0.6 mm, element: 0.5 mm) placed on the surface of the weld, centrally with respect to the middle defect. This is the simplest test case, where the target of the inversion is a single orientation angle. This means that the objective function depends only on one variable and that the gradient of the objective function is a sum of contributions from all cells. The top and bottom surfaces of the model were

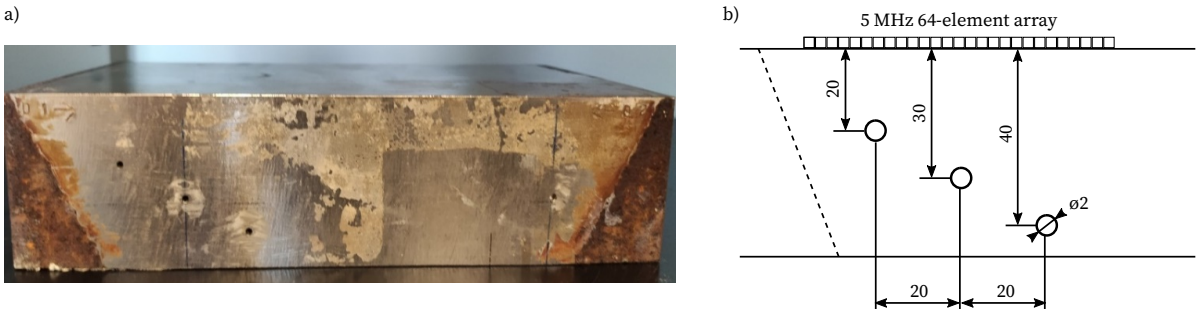

Figure 10: Schematic diagram for experimental weld map tomography on an EDF Inconel 182 V-weld with uniform orientations: a) photograph; b) experimental setup.

not exactly parallel, which was accounted for in the forward model underlying inversion. Since the pulse echo setup requires mirroring the computational domain, an arbitrary backwall profile can be defined, provided that the respective nodes belonging to the original and auxiliary domains are connected with zero-cost (zero-arrival-time) edges. This arrangement will be further demonstrated in Section 5.2.

The forward model underpinning inversion discretised the domain into $2 \times 2\,\mathrm{mm}$ cells, with each edge of a cell seeded with 10 nodes. For the parent material, we used $\rho_{\mathrm{parent}} = 8260\,\mathrm{kg\,m^{-3}}$, $c_{11} = 260\,\mathrm{GPa}$, $c_{12} = 100\,\mathrm{GPa}$, and $c_{44} = 80\,\mathrm{GPa}$. The weld material had the same density, and the elasticity matrix with $c_{11} = 265\,\mathrm{GPa}$, $c_{12} = 121\,\mathrm{GPa}$ $c_{13} = 140\,\mathrm{GPa}$, $c_{33} = 247\,\mathrm{GPa}$, $c_{44} = 112\,\mathrm{GPa}$, and $c_{66} = 86\,\mathrm{GPa}$. The latter was determined from the data provided by EDF.

As signalled in the preceding section, extracting time-of-arrival from real experimental data, is challenging. Scattering noise and the low amplitude of the backwall reflection preclude the use of simple automated methods, such as following the maximum of the Hilbert envelope. Fig. 11 shows an example of received signals across all array elements for a single excitation. The solid line represents extracted arrival time, whose small variations affect the inversion significantly. While the discussion on algorithms for determining arrival times is outside this paper's scope, we report using a method based on tracking the zero-crossing between two dominant extrema of the wave packet in this paper. Once the zero-point has been identified for all transducer pairs, we employed interpolation and the symmetry of the arrival time matrix to infer the values at missing points. The final result came from subtracting a constant offset, estimated on the cleanest time trace in the set, capturing the difference between the arrival time extracted using the AIC criterion and the previously chosen zero-crossing. While this procedure may appear complicated, it allowed for obtaining consistently satisfactory results for the examples considered in this paper.

Fig. 12 shows the results of the inversion, based on experimental time traces recorded at CEA. Weld map tomography started from uniform vertical orientation of grains and converged to $-8.11\,\mathrm{deg}$ after 9 iterations. Determining the exact angular error is not possible for this example, but the metallography performed on an off-cut of the same weld suggests the dominant orientation of $-8\,\mathrm{deg}$ which confirms that the inversion

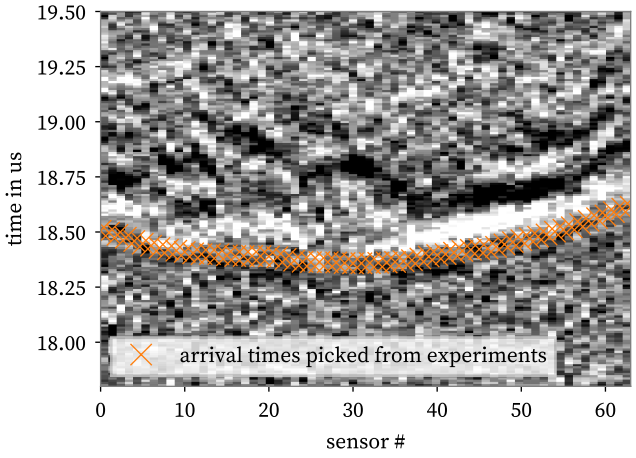

Figure 11: Extracting time-of-arrival as the target for inversion from experimental data (the map combines time traces across all sensors from single-transducer excitation; the markers show the identified times-of-arrival).

reached a realistic value. However, quantitative error analysis is possible for arrival times, as depicted in Fig. 12(b). The mean absolute error was 0.021 µs, the median absolute error – 0.015 µs, and the maximum absolute error – 0.093 µs. The highest errors are between transducers close to array extremities, suggesting that the geometry of the sample was not captured correctly. Despite that, the result of the tomography is close to the reference provided for the mock-up. We attribute this robustness to the fact that only a single orientation angle is sought for in this example, minimising the impact of locally mismatched definitions.

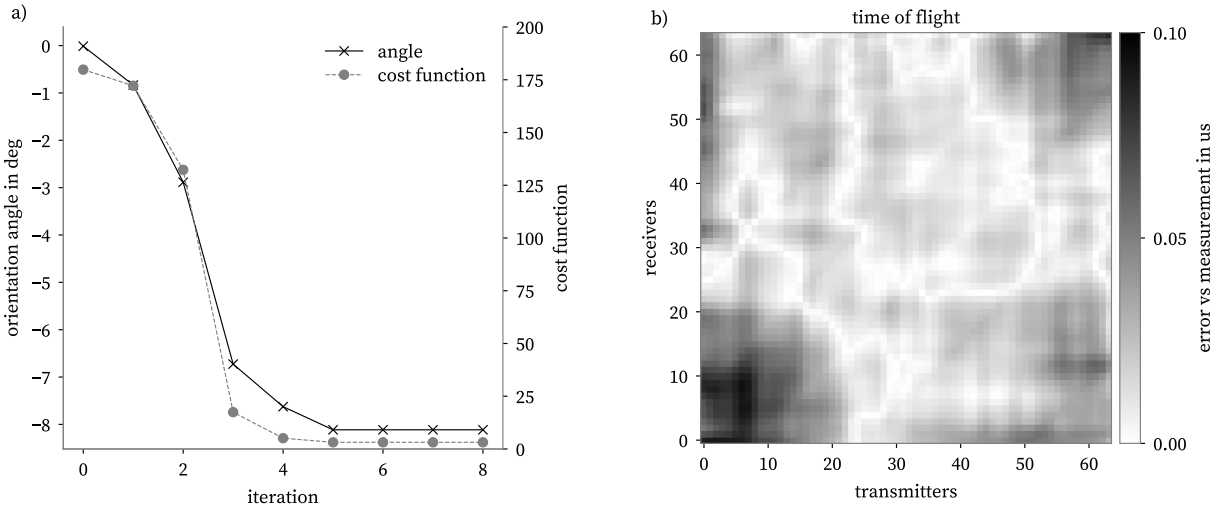

Figure 12: Results of weld map tomography for the uniform Inconel weld: a) cost function and orientation angle at different iterations; b) a map of absolute time-of-flight errors ($|\tau_{\text{original}} - \tau_{\text{inversion}}|$).

The practically relevant verification of the inversion is to perform imaging with the obtained material information. We used the classical total focusing method (TFM) [26] which is a modified, Hilber-envelope-

based version of the beamforming algorithm. The imaging function $I(x, y)$ is defined as

$$I(x,y) = \left| \sum_{i=1}^{M} \sum_{j=1}^{M} \mathrm{H}\left[u_{i,j} \left(\tau_{i\to(x,y)} + \tau_{j\to(x,y)} \right) \right] \right| \tag{13}$$

where (x, y) is the position in the physical domain, M is the number of elements in the array, $u_{i,j}$ is the response measured by element i with element j exciting, $\tau_{i\to(x,y)}$ is the traveltime between element i and point (x, y) (called a delay law) and H[] is the Hilbert transform.

Fig. 13 shows TFM images calculated using the same dataset as the one used for inversion. For comparison, we show the 'conventional' image evaluated under the assumption that the material is isotropic, and the 'updated' image which uses the results from inversion presented earlier. Both images are normalised to the maximum amplitude of the middle defect (individually). The circular markers indicate true positions of side drilled holes. To quantify the difference between the two images we calculated the signal-to-noise ratio (SNR) using the following procedure. First, the algorithm searched for a maximum within +/- 5 mm of the known defect position. Then, we defined a signal region I_{sig} (solid line square), and the noise probe region I_{noise} (dashed line square), which were squares with sides 4 and 10 mm, respectively, centred around the maximum. The SNR was calculated using the maximum amplitude in the signal region and the root-mean-square amplitude in the noise region (not including the signal part)

$$\mathrm{SNR} = 20 \log_{10} \frac{\max(I_{\mathrm{sig}})}{\sqrt{\overline{I_{\mathrm{noise}}^2}}} \tag{14}$$

The results in Fig. 13 confirm that using the correct material information reduces the overall level of noise in the image, improves the location of defect signatures (by 3.2, 1.1 and 4.6 mm from the left to the right defect, and enhances the SNR (by 5.9, 14.4, and 7.5 dB, respectively), making defect signatures more focused and better pronounced. Moreover, it confirms the effectiveness of weld map tomography and the benefits it provides to imaging.

5.2. Weld with a non-planar backwall

In this section we test weld map tomography on a 316L stainless steel industrial mock-up from EDF. The sample has a typical V-shaped configuration and a non-planar backwall profile. Two target defects (side-drilled holes of 1 mm diameter) located at the centreline (approximately 10 and 20 mm from the top surface) provide a reference for imaging. Compared to the previous sample, the growth of complexity is twofold: first, we update individual local grain orientations; second, the backwall profile has a non-planar profile.

The measurements, taken at CEA, used a contact 5 MHz 64-element array with 0.6 mm pitch and 0.5 mm element width, positioned centrally above the weld. Extracting backwall-reflected arrival times from the recorded dataset required a semi-manual procedure described in Section 5.1. Weld map tomography, as

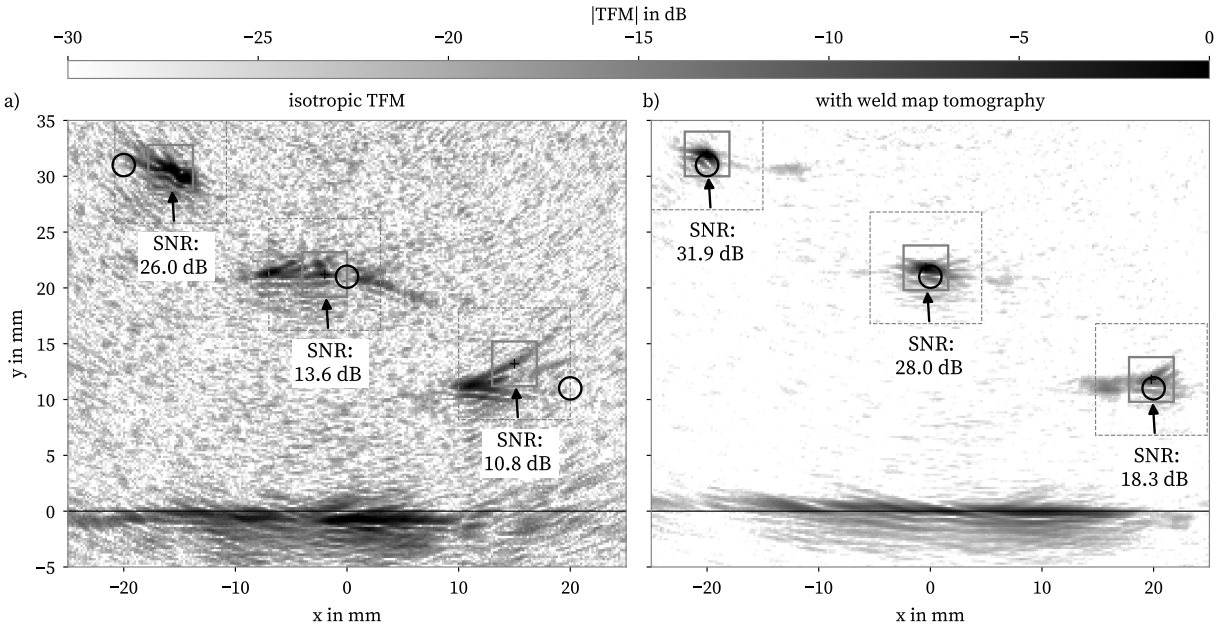

Figure 13: Total focusing method imaging with material information: a) standard isotropic delay laws; b) with delay laws coming from weld map tomography. The SNRs of the defect signatures indicated for comparison.

presented in this paper, focuses on determining local grain orientations, that is, material information only. Thus, the geometry was fixed and assumed known, which is a straightforward task for a mock-up. Since this paper focuses on updating material properties, keeping the geometry fixed, we omit the simplified representation of the backwall profile for brevity.

The forward model used in the inversion discretised the domain into $2 \times 2\,\text{mm}$ cells, seeded with ten nodes per each side. For the parent material, we used $\rho_{\text{parent}} = 7800\,\text{kg}\,\text{m}^{-3}$, $c_{11} = 276\,\text{GPa}$, $c_{12} = 102\,\text{GPa}$, and $c_{44} = 87\,\text{GPa}$. The weld material had the same density, and the elasticity matrix with $c_{11} = 245\,\text{GPa}$, $c_{12} = 110\,\text{GPa}$, $c_{13} = 145\,\text{GPa}$, $c_{22} = 253\,\text{GPa}$, $c_{33} = 221\,\text{GPa}$, $c_{44} = 110\,\text{GPa}$, and $c_{66} = 75\,\text{GPa}$ [17]. We exercised the two-stage inversion, identical to that in Section 4, where the first stage looks for the optimal dominant orientation angle for the generalised Ogilvy model, and the second stage updates local orientations to further decrease the cost function until convergence.

Fig. 14 shows the results of the inversion which started from an Ogilvy map with 0° dominant orientation. After six iteration the minimisation converged to $-20.5°$ and moved to the second stage where individual angles were further updated, completing after a total of 19 iterations. The evolution of the cost function clearly suggests that the dominant grain orientation had the most significant effect on the inversion.

The arrival time errors are higher than in the previous example, with the mean absolute error of $0.034\,\mu\text{s}$, the median absolute error of $0.029\,\mu\text{s}$, and the maximum absolute error of $0.185\,\mu\text{s}$. It is worth noting that the 'white spots' in Fig. 14(b) indicate that for these transducer pairs it was not possible to extract arrival

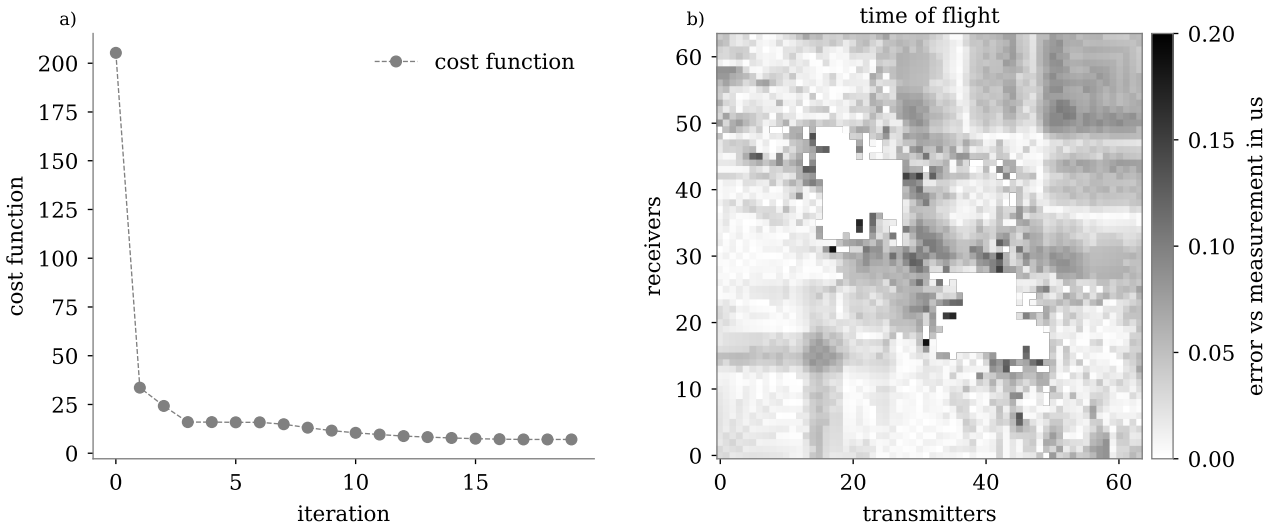

Figure 14: Results of weld map tomography for the stainless steel weld with a non-planar backwall: a) cost function and orientation angle at different iterations; b) a map of absolute time-of-flight errors ($|\tau_{\text{original}} - \tau_{\text{inversion}}|$).

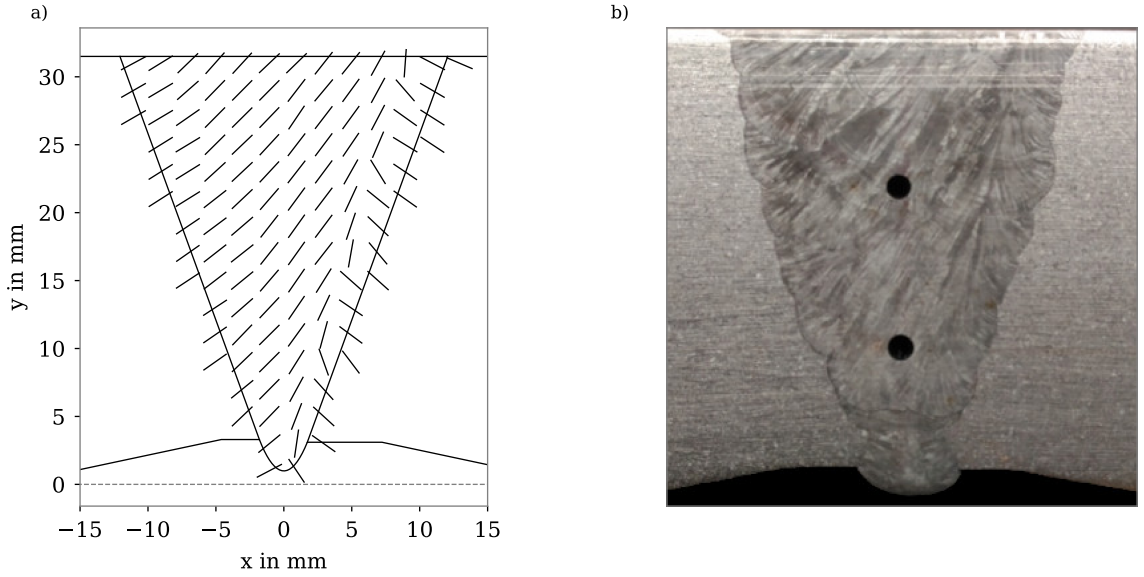

Figure 15: Results of weld map tomography for the stainless steel weld with a non-planar backwall: a) updated local grain orientations; b) the metallography image of the mock-up.

times from the measured data. While this reduction in the available data is undesired for the inversion, this case confirms that weld map tomography does not require the full dataset to work. We also observe that the maximum errors occured for transducer pairs close to the undefined arrival time regions, bound by high uncertainty. The mean error is still low and represents a practically promising performance. In Fig. 15 we offer a visual comparison of the updated orientations with the metallography of the mock-up, confirming

the effectiveness of the inversion.

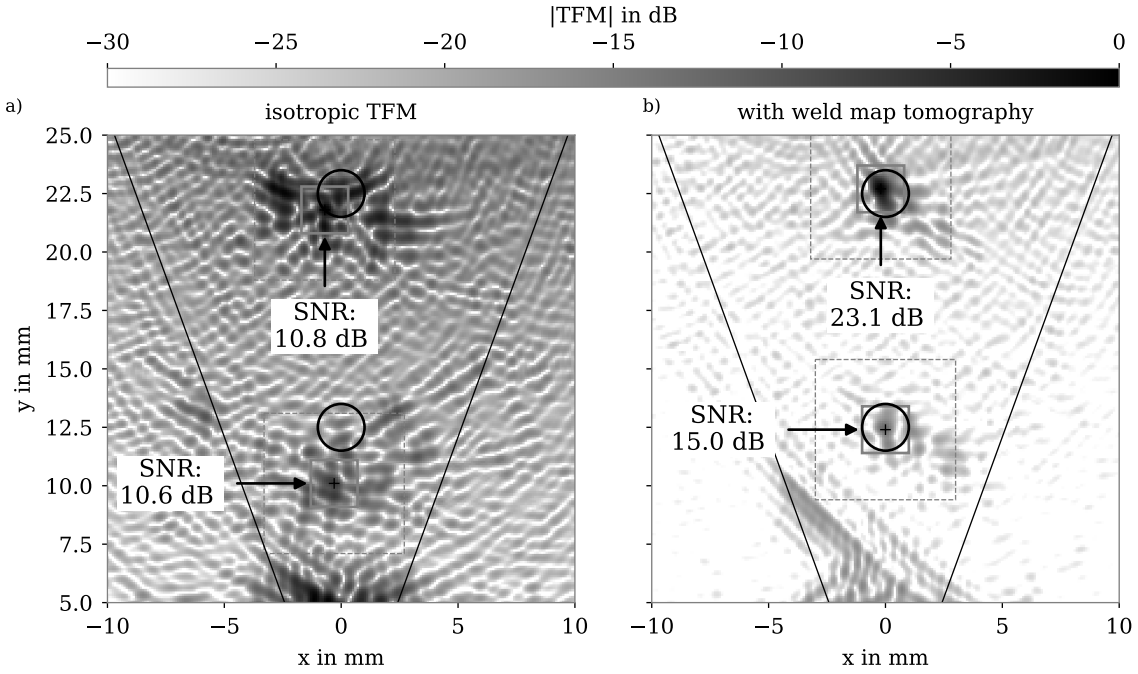

Figure 16: Total focusing method imaging with material information for the stainless steel weld with a non-planar backwall: a) standard isotropic delay laws; b) with delay laws coming from weld map tomography. The SNRs of the defect signatures indicated for comparison.

The final verification involves calculating the TFM image using the same recorded dataset with and without material information provided by weld map tomography, as shown in Fig. 16. Updated material information reduces the noise in the image and improves the prominence and focus of defect signatures. While the noise is not eliminated entirely, the SNRs of the target defects improve by 12.3 and 4.4 dB, respectively. We acknowledge artefacts close to the root of the weld; however, their origin, and ways for reducing them, remain the subject of future work. Nevertheless, our proposed inversion technique output local orientations visually agreeing well with the metallography image and providing good enhancement to the ultrasonic image of target defects, despite the complex backwall geometry.

5.3. ADVISE mock-up

The final example considered is an austenitic stainless steel mock-up manufactured for the project sponsoring this work. Project partners designed and manufactured a weld of industrial relevance, but with careful recording of welding parameters, materials, and other details necessary for weld formation and phenomenological MINA [2] modelling.

The mock-up was manufactured by joining two stainless steel pipes (1.4550) with wall thickness of 39 mm (outside diameter: 517 mm) - Fig. 17. The circumferential weld, in the flat position, was manufactured

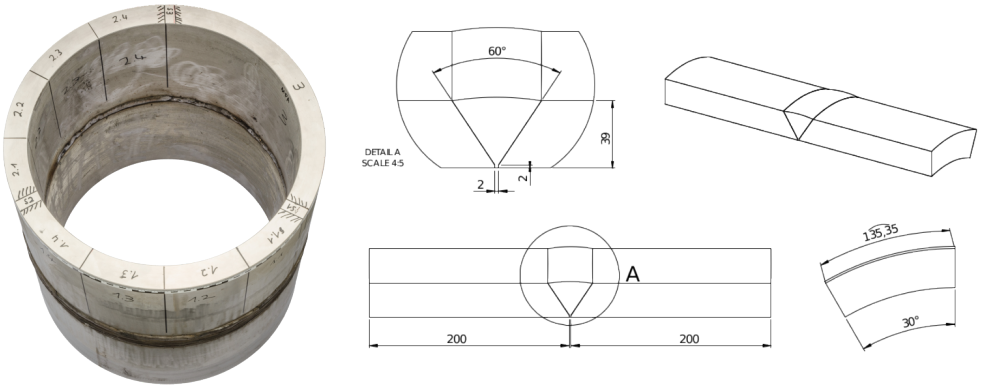

Figure 17: The ADVISE WP2 mock-up: a photograph and schematic drawings of a cut out section.

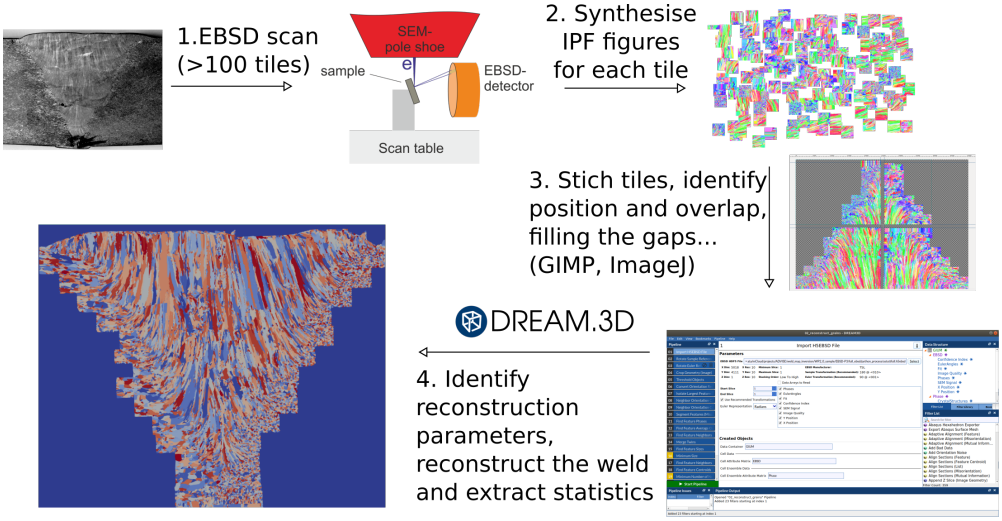

Figure 18: The workflow for the reconstruction of the microstructure from EBSD measurements.

using the shielded metal arc method with ESAB OK 61.30 filler (1.4316). The cylindrical specimen was then sectioned into several parts along the circumference (Fig. 17), which served other research tasks.

One section of the mock-up was used for material examinations, both traditional metallography and EBSD. For the EBSD measurement, the weld was further sectioned into four parts and each was covered by a grid of smaller measurement areas in the microscope. The obtained dataset, comprising over 100 'tiles' was stitched and analysed using Dream.3D [27], an open-source package for microstructure synthesis, to deliver a numerical microstructure, that can be visualised, analysed, and subsequently used in further modelling or the verification of experimental inversion.

To facilitate measurements, the top and bottom surfaces of the mock-up were machined to achieve flat surface (Fig. 19). This modification helped ensure good contact between the transducer and the sample and allowed focusing on the inversion, rather than the transducer issues. Material evaluations at the University

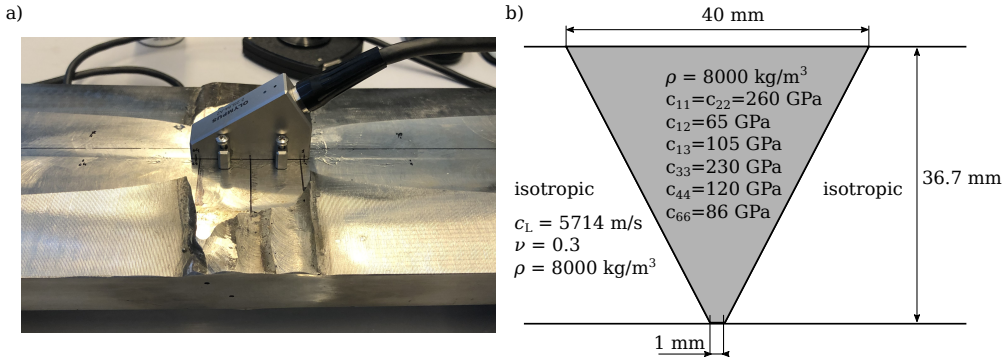

Figure 19: ADVISE WP2 mock-up and the transducer used in weld map tomography: a) a photograph; b) dimensions with material properties.

of Stuttgart indicated several natural defects within the weld and additional targets (holes) were drilled along the chamfer at CEA.

Array measurements using a 64-element, 0.75 mm 2.25 MHz transducer (in contact with the sample, directly on top of the weld, coupled through silicone gel) were taken at KTU using the Gekko system from Eddyfi. The acquisitions were processed using the semi-manual time-of-arrival extraction procedure described in Section 5.1, yielding the target for the weld map tomography algorithm.

The forward model used in inversion assumed known material properties of the sample and known geometry. We used the EBSD dataset to execute homogenisation and determine the macroscopic transversely isotropic elastic tensor based on the grain structure and the crystal elastic tensor. These parameters are listed in Fig. 19.

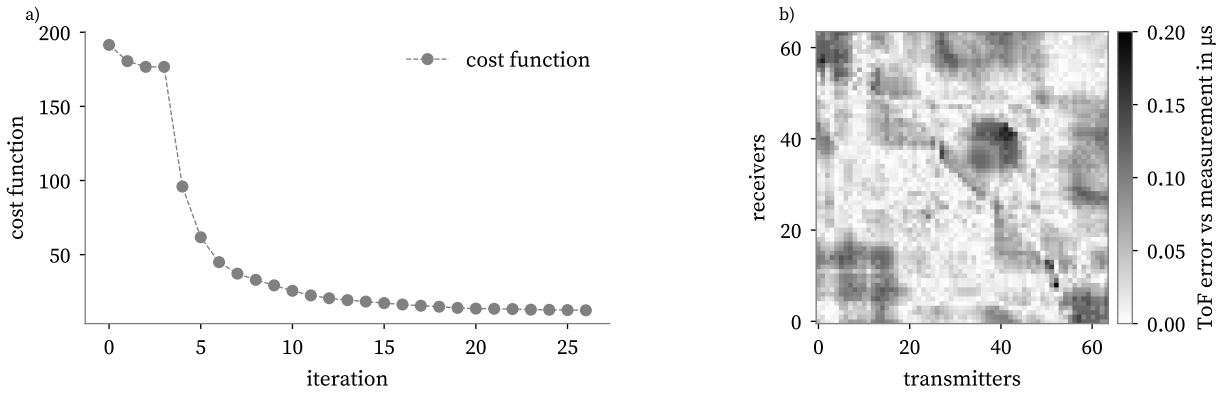

Figure 20: Results of weld map tomography for the stainless steel ADVISE mock-up: a) cost function and orientation angle at different iterations; b) a map of absolute time-of-flight errors ($|\tau_{\text{original}} - \tau_{\text{inversion}}|$).

Two-stage weld map tomography, analogous to that in Section 4, converged after 26 iterations, with the first stage (updating the dominant orientation of the generalised Ogilvy map) taking four iterations. Fig. 20 shows the cost function and the final map of absolute time of flight errors (mean absolute error: 0.044 µs, median absolute error: 0.036 µs, and maximum absolute error: 0.193 µs). To further illustrate the

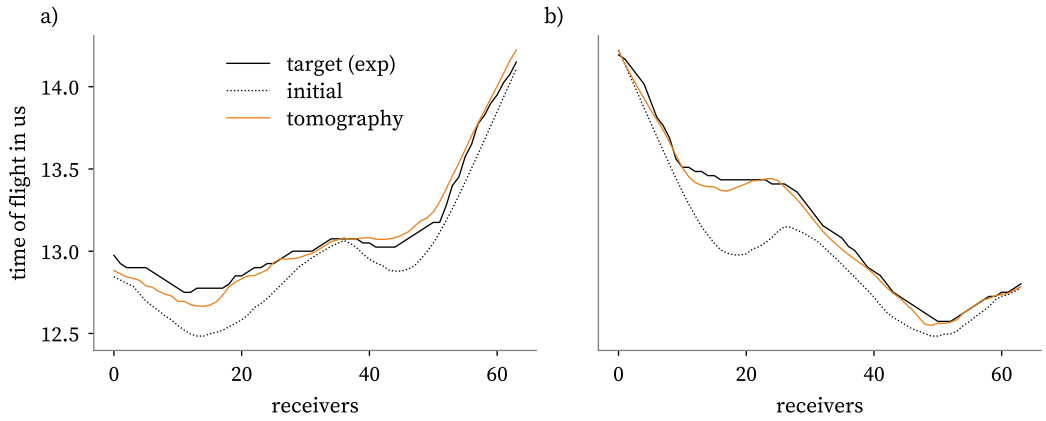

Figure 21: Evolution of the time-of-flight between the initial guess and the converged weld map tomography output vs the target: a) source at transducer #13; b) source at transducer #53.

evolution of the time-of-flight map during inversion, we show the initial, the final, and the target results for two sources in Fig. 21. In the illustrated cases, initial time-of-flight errors were up to 0.5 µs for some receivers, while reducing to less than 0.1 µs in the final result.

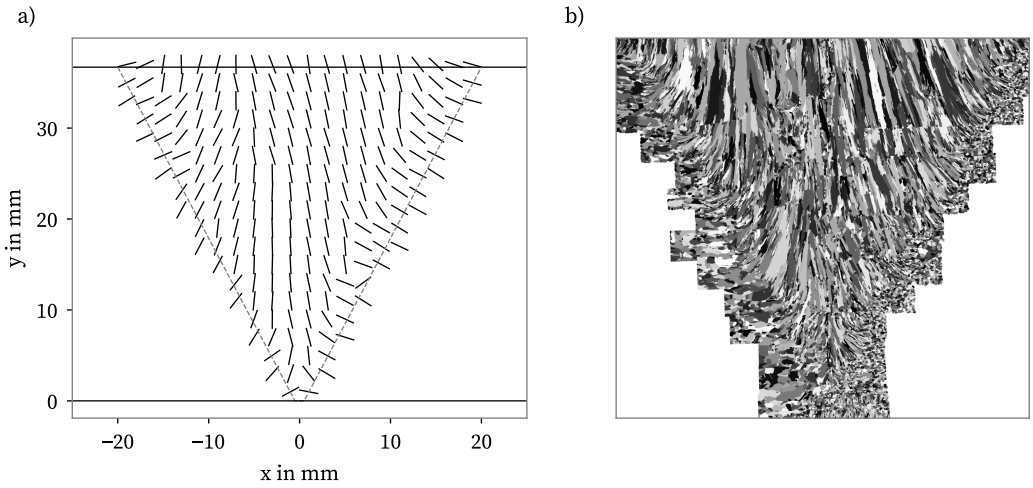

Figure 22: Results of weld map tomography for the stainless steel ADVISE mock-up: a) updated local grain orientations; b) microstructure reconstruction based on EBSD measurements.

Fig. 22 compares grain orientations determined using weld map tomography and the reconstruction of the EBSD measurement taken at the University of Stuttgart. This visual comparison gives a convincing indication of the effectiveness of the method. We note that the errors in orientation angles are mainly concentrated around the chamfer, where the EBSD data had low confidence index. Nevertheless, as in previously presented examples, the final confirmation of the efficacy of weld map tomography is illustrated by applying its output to imaging.

The TFM imaging used the dataset as that produced the time-of-flight target for inversion. Fig. 23 compares images calculated: a) using the conventional isotropic assumption and b) delay laws based on the output of weld map tomography. The effect of the proposed inversion technique is clear and convincing. First, the sample had two known target defects (side-drilled holes) along the right chamfer - Fig. 23 shows that only one is visible in the conventional TFM image. Including material information coming from inversion raised the bottom chamfer defect from the background noise. The SNRs of the chamfer defects improved by around 4 and 8 dB. We note that if a defect signature is not present in the conventional image, the SNR value has no meaning (as there is no 'signal'); nevertheless, it is calculated in the image for completeness.

Additionally to the intentionally introduced side-drilled holes, two natural defect signatures emerged in Fig. 23b) - one close to the centreline and another in the vicinity of the chamfer. Post-manufacture X-ray scans of the weld indicated the presence of voids in some parts of the weld and it is confirmed with ultrasonic imaging. More importantly, the absence of these natural defects' signatures in the conventional image proves the effectiveness of weld map tomography in supporting imaging and is a compelling proof of the importance of accounting for material information.

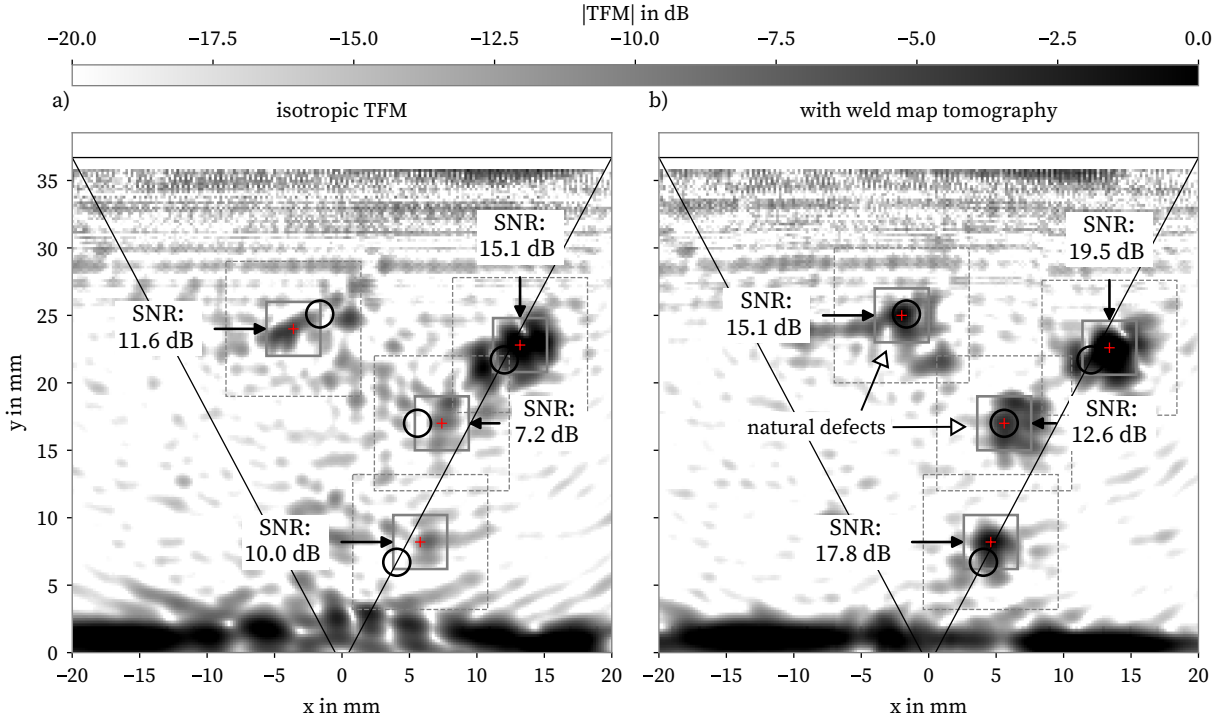

Figure 23: Total focusing method imaging with material information for the ADVISE mock-up: a) standard isotropic delay laws; b) with delay laws coming from weld map tomography. The SNRs of the defect signatures indicated for comparison.

6. Conclusions

This paper proposed a method for determining local grain orientations in complex, thick welds from ultrasonic array data. The reconstruction followed the ray tomography principle, accounting for the heterogeneous anisotropy of the welds of interest. The inversion used a shortest-ray-path model as the forward solver and the paper detailed the principles and construction of the model. We discussed the importance of the a priori information about the weld and the advantages of using simple geometrical descriptions for initial stages of inversion. The algorithm was first showcased using a numerical example based on an industrial inspection scenario, with grain-scale time-domain finite element simulations acting as a virtual experiment. The results of the inversion showed good agreement with the numerically generated microstructure. Encouraged by this result, we demonstrated weld map tomography on three mock-ups - two supplied by the industry, and one manufactured specifically for this research. The outcome of the method compared favourably with destructive material examinations (both metalography and EBSD) and provided the input for updating the delay laws for imaging. In all examples, TFM images using material information from inversion showed significant improvement of both the location of defect signatures and SNR, confirming the efficacy of the proposed algorithm.

Acknowledgement

This research was a part of the ADVISE project (www.advise-h2020.eu) funded from the Euratom research and training programme 2014-2018 under grant agreement no. 755500.

Appendix A. Generalised Ogilvy map

The geometric description of grain orientations proposed by Ogilvy [3] is a simple but powerful method. Throughout recent decades it became the gold standard for modelling local orientations in austenitic stainless steel welds. This paper uses a slightly extended version of the Ogilvy map, accounting for the dominant orientation angle which is relatively common in published examinations (see e.g. Fig. 10a)). What is presented below is conceptually analogous to an approach used in [17].

Let us start from the classical Ogilvy map [3] for completeness. We consider a simple V-weld, of thickness a, left and right weld angles α_L and α_R, and weld bead lengths (positive) d_L and d_R. For a domain defined in $y - z$ coordinates with z being the vertical, the Ogilvy model requires four parameters: T_L and T_R, representing the tangent of the orientation angles at the left and right chamfers, and η_L and eta_R, representing the rate of change of the angle while moving horizontally from the chamfer towards the centreline (where the grains are always vertical). The setup, the coordinate system, and the parameters are illustrated in Fig. A.1. Our convention assumes the lengths, weld angles, and η parameters to be always

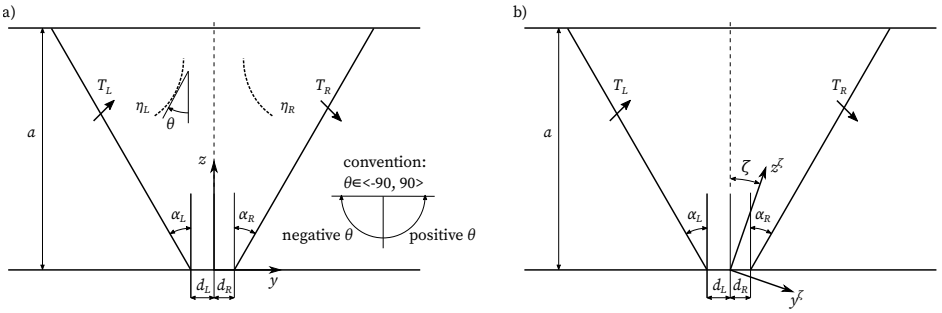

Figure A.1: Schematic diagram for: a) the classical Ogilvy model; b) auxiliary rotation of the coordinate system to account for dominant orientation ζ.

positive. Orientation tangent T_L is expected to be positive, while T_R - to be negative. It is common to assume symmetry, with $T_L = -T_R$, $\eta_L = \eta_R$, $\alpha_L = \alpha_R$, and $d_L = d_R$.

Grain orientations θ defined as the rotation from the vertical positive anticlockwise are calculated using the following expressions

$$\theta(y,z) = \begin{cases} \arctan\left(\frac{T_L|d_L + z\tan\alpha_L|}{y^{\eta_L}}\right) - \frac{\pi}{2}, & \text{if } y < 0 \\ \arctan\left(\frac{T_R|d_R + z\tan\alpha_R|}{y^{\eta_R}}\right) + \frac{\pi}{2}, & \text{if } y > 0 \\ 0, & \text{if } y = 0 \end{cases} \tag{A.1}$$

The generalised Ogilvy map, as we call it in this paper, adds one more parameter ζ to capture the dominant orientation representing the direction of privileged grain growth during cooling [17]. This parameter is the angle between the original z-axis and the new axis along which the grains would align. In the model, we account for that by temporarily rotating the y-z system by ζ (see Fig. A.1b)). If $|\zeta|$ is greater than α_L or α_R it should be capped at the weld angle for the coordinate rotation (for some configurations, e.g. very narrow welds, the limit may need to be less than the weld angle). After the rotation, each point in the original y-z reference frame has its auxiliary counterpart in the y^ζ-z^ζ frame. Then, the grain orientations are calculated as:

$$\theta(y,z) = \begin{cases} \arctan\left(\frac{T_L\left|d_L + z^\zeta\tan\left(\alpha_L - \zeta\right)\right|}{(y^\zeta)^{\eta_L}}\right) - \frac{\pi}{2} + \zeta, & \text{if } y^\zeta < 0 \\ \arctan\left(\frac{T_R\left|d_R + z^\zeta\tan\left(\alpha_R + \zeta\right)\right|}{(y^\zeta)^{\eta_R}}\right) + \frac{\pi}{2} + \zeta, & \text{if } y^\zeta > 0 \\ \zeta, & \text{if } y^\zeta = 0 \end{cases} \tag{A.2}$$

When applying the dominant orientation parameter ζ to an originally symmetric weld (with $T_L = -T_R$), one should adjust these parameters to retain relevance to realistic cases. A rule-of-thumb adjustment based on comparing such maps to metallography images suggests multiplying initial T_L and T_R parameters by $(1 + 0.01\zeta)$ and $(1 - 0.01\zeta)$ respectively.

Appendix B. Orientation and material properties conventions

The inversion algorithm and the SRP forward model proposed in this paper rely on a macroscopic representation of the weld, in which local properties are governed by a transversely isotropic material rotated according to the orientation angle. The rotation is such that the 'soft' axis of the material aligns with the orientation direction. The SRP forward model and weld map tomography are set up in the y-z domain, hence the 'soft' axis will be the 33 material direction. If an analogous calculation was performed in the x-y domain, e.g. in a 2D finite element simulation, one would need to appropriately rotate the material stiffness tensor, so that the 'soft' axis will appear as the 22 material direction.

References

[1] G. D. Connolly, M. J. S. Lowe, J. A. G. Temple, S. I. Rokhlin, The application of Fermat's principle for imaging anisotropic and inhomogeneous media with application to austenitic steel weld inspection, Proceedings of the Royal Society A: Mathematical, Physical and Engineering Sciences 465 (2009) 3401–3423. doi:10.1098/rspa.2009.0272.

[2] J. Moysan, A. Apfel, G. Corneloup, B. Chassignole, Modelling the grain orientation of austenitic stainless steel multipass welds to improve ultrasonic assessment of structural integrity, International Journal of Pressure Vessels and Piping 80 (2003) 77–85. doi:10.1016/S0308-0161(03)00024-3.

[3] J. A. Ogilvy, Computerized ultrasonic ray tracing in austenitic steel, NDT International 18 (1985) 67–77. doi:10.1016/0308-9126(85)90100-2.

[4] B. Chassignole, R. El Guerjouma, M.-A. Ploix, T. Fouquet, Ultrasonic and structural characterization of anisotropic austenitic stainless steel welds: Towards a higher reliability in ultrasonic non-destructive testing, NDT & E International 43 (2010) 273–282. doi:10.1016/j.ndteint.2009.12.005.

[5] A. J. Hunter, B. W. Drinkwater, J. Zhang, P. D. Wilcox, D. O. Thompson, D. E. Chimenti, A study into the effects of an austenitic weld on ultrasonic array imaging performance, 2011, pp. 1063–1070. doi:10.1063/1.3592054.

[6] A. F. Mark, Z. Fan, F. Azough, M. J. S. Lowe, P. J. Withers, Investigation of the elastic/crystallographic anisotropy of welds for improved ultrasonic inspections, Materials Characterization 98 (2014) 47–53. doi:10.1016/j.matchar.2014.09.012.

[7] M. Spies, Modeling of transducer fields in inhomogeneous anisotropic materials using Gaussian beam superposition, NDT & E International 33 (2000) 155–162. doi:10.1016/S0963-8695(99)00036-5.

[8] K. J. Langenberg, R. Hannemann, T. Kaczorowski, R. Marklein, B. Koehler, C. Schurig, F. Walte, Application of modeling techniques for ultrasonic austenitic weld inspection, NDT & E International 33 (2000) 465–480. doi:10.1016/S0963-8695(00)00018-9.

[9] C. Gueudre, L. Le Marrec, J. Moysan, B. Chassignole, Direct model optimisation for data inversion. Application to ultrasonic characterisation of heterogeneous welds, NDT & E International 42 (2009) 47–55. doi:10.1016/j.ndteint.2008.07.003.

[10] Z. Fan, A. F. Mark, M. J. S. Lowe, P. J. Withers, Nonintrusive estimation of anisotropic stiffness maps of heterogeneous steel welds for the improvement of ultrasonic array inspection, IEEE Transactions on Ultrasonics, Ferroelectrics, and Frequency Control 62 (2015) 1530–1543. doi:10.1109/TUFFC.2015.007018.

[11] J. Zhang, A. Hunter, B. W. Drinkwater, P. D. Wilcox, Monte carlo inversion of ultrasonic array data to map anisotropic weld properties, IEEE Transactions on Ultrasonics, Ferroelectrics, and Frequency Control 59 (2012) 2487–2497. doi:10.1109/TUFFC.2012.2481.

[12] K. M. M. Tant, E. Galetti, A. J. Mulholland, A. Curtis, A. Gachagan, A transdimensional Bayesian approach to ultrasonic travel-time tomography for non-destructive testing, Inverse Problems 34 (2018) 095002. doi:10.1088/1361-6420/aaca8f.

[13] K. M. M. Tant, E. Galetti, A. J. Mulholland, A. Curtis, A. Gachagan, Effective grain orientation mapping of complex and locally anisotropic media for improved imaging in ultrasonic non-destructive testing, Inverse Problems in Science and Engineering 28 (2020) 1694–1718. doi:10.1080/17415977.2020.1762596.

[14] J. Singh, K. Tant, A. Mulholland, C. MacLeod, Deep Learning Based Inversion of Locally Anisotropic Weld Properties from Ultrasonic Array Data, Applied Sciences 12 (2022) 532. doi:10.3390/app12020532.

[15] J. Singh, K. Tant, A. Curtis, A. Mulholland, Real-time super-resolution mapping of locally anisotropic grain orientations for ultrasonic non-destructive evaluation of crystalline material, Neural Computing and Applications 34 (2022) 4993–5010. doi:10.1007/s00521-021-06670-8.

[16] C. Ménard, S. Robert, R. Miorelli, D. Lesselier, Optimization algorithms for ultrasonic array imaging in homogeneous anisotropic steel components with unknown properties, NDT & E International 116 (2020) 102327. doi:10.1016/j.ndteint.2020.102327.

[17] C. Menard, S. Robert, D. Lesselier, Ultrasonic Array Imaging of Nuclear Austenitic V-Shape Welds with Inhomogeneous and Unknown Anisotropic Properties, Applied Sciences 11 (2021) 6505. doi:10.3390/app11146505.

[18] A. Hormati, I. Jovanović, O. Roy, M. Vetterli, Robust ultrasound travel-time tomography using the bent ray model, in: Medical Imaging 2010: Ultrasonic Imaging, Tomography, and Therapy, volume 7629, SPIE, 2010, pp. 165–176. doi:10.1117/12.844693.

[19] O. Nowers, D. J. Duxbury, J. Zhang, B. W. Drinkwater, Novel ray-tracing algorithms in NDE: Application of Dijkstra and A∗ algorithms to the inspection of an anisotropic weld, NDT & E International 61 (2014) 58–66. doi:10.1016/j.ndteint.2013.08.002.

[20] O. Nowers, D. J. Duxbury, B. W. Drinkwater, Ultrasonic array imaging through an anisotropic austenitic steel weld using an efficient ray-tracing algorithm, NDT & E International 79 (2016) 98–108. doi:10.1016/j.ndteint.2015.12.009.

[21] P. Virtanen, R. Gommers, T. E. Oliphant, M. Haberland, T. Reddy, D. Cournapeau, E. Burovski, P. Peterson, W. Weckesser, J. Bright, S. J. van der Walt, M. Brett, J. Wilson, K. J. Millman, N. Mayorov, A. R. J. Nelson, E. Jones, R. Kern, E. Larson, C. J. Carey, İ. Polat, Y. Feng, E. W. Moore, J. VanderPlas, D. Laxalde, J. Perktold, R. Cimrman, I. Henriksen, E. A. Quintero, C. R. Harris, A. M. Archibald, A. H. Ribeiro, F. Pedregosa, P. van Mulbregt, SciPy 1.0 Contributors, SciPy 1.0: Fundamental Algorithms for Scientific Computing in Python, Nature Methods 17 (2020) 261–272. doi:10.1038/s41592-019-0686-2.

[22] P. Huthwaite, Quantitative Imaging with Mechanical Waves, Ph.D. thesis, Imperial College London, 2012.

[23] P. Huthwaite, Accelerated finite element elastodynamic simulations using the GPU, Journal of Computational Physics 257 (2014) 687–707. doi:10.1016/j.jcp.2013.10.017.

[24] R. Quey, P. R. Dawson, F. Barbe, Large-scale 3D random polycrystals for the finite element method: Generation, meshing and remeshing, Computer Methods in Applied Mechanics and Engineering 200 (2011) 1729–1745. doi:10.1016/j.cma.2011.01.002.

[25] A. St-Onge, Akaike information criterion applied to detecting first arrival times on microseismic data, in: SEG Technical Program Expanded Abstracts 2011, SEG Technical Program Expanded Abstracts, Society of Exploration Geophysicists, 2011, pp. 1658–1662. doi:10.1190/1.3627522.

[26] C. Holmes, B. W. Drinkwater, P. D. Wilcox, Post-processing of the full matrix of ultrasonic transmit–receive array data for non-destructive evaluation, NDT & E International 38 (2005) 701–711. doi:10.1016/j.ndteint.2005.04.002.

[27] M. A. Groeber, M. A. Jackson, DREAM.3D: A Digital Representation Environment for the Analysis of Microstructure in 3D, Integrating Materials and Manufacturing Innovation 3 (2014) 56–72. doi:10.1186/2193-9772-3-5.